Two-Dimensional Arrays of Transition Metal Nitride Nanocrystals

Xu Xiao, Hao Wang, Weizhai Bao, Patrick Urbankowski, Long Yang, Yao Yang, Kathleen Maleski, Linfan Cui, Simon J. L. Billinge, Guoxiu Wang, and Yury Gogotsi*

The synthesis of low-dimensional transition metal nitride (TMN) nanomaterials is developing rapidly, as their fundamental properties, such as high electrical conductivity, lead to many important applications. However, TMN nanostructures synthesized by traditional strategies do not allow for maximum conductivity and accessibility of active sites simultaneously, which is a crucial factor for many applications in plasmonics, energy storage, sensing, and so on. Unique interconnected two-dimensional (2D) arrays of few-nanometer TMN nanocrystals not only having electronic conductivity in-plane, but also allowing transport of ions and electrolyte through the porous nanosheets, which are obtained by topochemical synthesis on the surface of a salt template, are reported. As a demonstration of their application in a lithium–sulfur battery, it is shown that 2D arrays of several nitrides can achieve a high initial capacity of >1000 mAh g^{-1} at 0.2 C and only about 13% degradation over 1000 cycles at 1 C under a high areal sulfur loading (>5 mg cm^{-2}).

Due to the recent demonstration of promising properties of transition metal nitride (TMN) nanomaterials in fields ranging from plasmonics to energy harvesting, conversion, and storage, the research of TMN nanomaterials has attracted attention, especially with regard to the development of new synthesis techniques and material applications.[1–5] As a typical example, there are two major challenges remaining in the cathodes of lithium–sulfur (Li–S) batteries—full utilization of sulfur and strong affinity between host materials and sulfur species.[6] Recently, TMNs have been validated to have a

stronger interaction with sulfur species, when compared to widely studied carbon materials.[6,7] Combined with high electrical conductivity, TMN nanomaterials can help alleviate challenges. However, it should be noted that the previous reports of promising performance of Li–S batteries were mainly achieved on low areal sulfur loading (below 3 mg cm^{-2}),[8] while reaching the high and stable capacity during long-term cycling (>500 cycles) is still challenging but highly demanded for high areal sulfur loading, which is critical for providing sufficient volumetric energy densities for battery-powered electric vehicles (BEVs).[9] This is due to the fact that the structure and conductivity cannot be optimized simultaneously in conventional synthesis methods, which is also a common issue in many research fields.

In general, zero-dimensional (0D) nanoparticles with very high surface area can provide highly exposed active sites.[10,11] However, electron transport severely decreases if there are only physical contacts between self-assembled nanocrystals. On the other hand, two-dimensional (2D) metallically conducting flakes can serve as conductive platforms for the less conducting material at their surface. For instance, a restacked MXene film was reported to have an excellent conductivity, up to 8000 S cm^{-1}.[12] Nevertheless, such a dense film (3–4 g cm^{-3}) is not favorable for ultrahigh rate ion transport.[13,14] Designing

Dr. X. Xiao, Dr. H. Wang, Dr. W. Bao, Dr. P. Urbankowski, K. Maleski, Dr. L. Cui, Prof. Y. Gogotsi
Department of Materials Science and Engineering and A. J. Drexel Nanomaterials Institute
Drexel University
Philadelphia, PA 19104, USA
E-mail: gogotsi@drexel.edu
L. Yang, Prof. S. J. L. Billinge
Department of Applied Physics and Applied Mathematics
Columbia University
New York, NY 10027, USA
Y. Yang
Department of Chemistry and Chemical Biology
Cornell University
Ithaca, NY 14853, USA

Dr. H. Wang
Soochow Institute for Energy and Materials Innovations
College of Energy
Soochow University
Suzhou 215006, China
Dr. W. Bao, Prof. G. Wang
Centre for Clean Energy Technology
School of Mathematical and Physical Sciences
University of Technology Sydney
Sydney, NSW, Australia
Prof. S. J. L. Billinge
Condensed Matter Physics and Materials Science Department
Brookhaven National Laboratory
Upton, NY 11973, USA

ADVANCED
SCIENCE NEWS
www.advancedsciencenews.com

ADVANCED
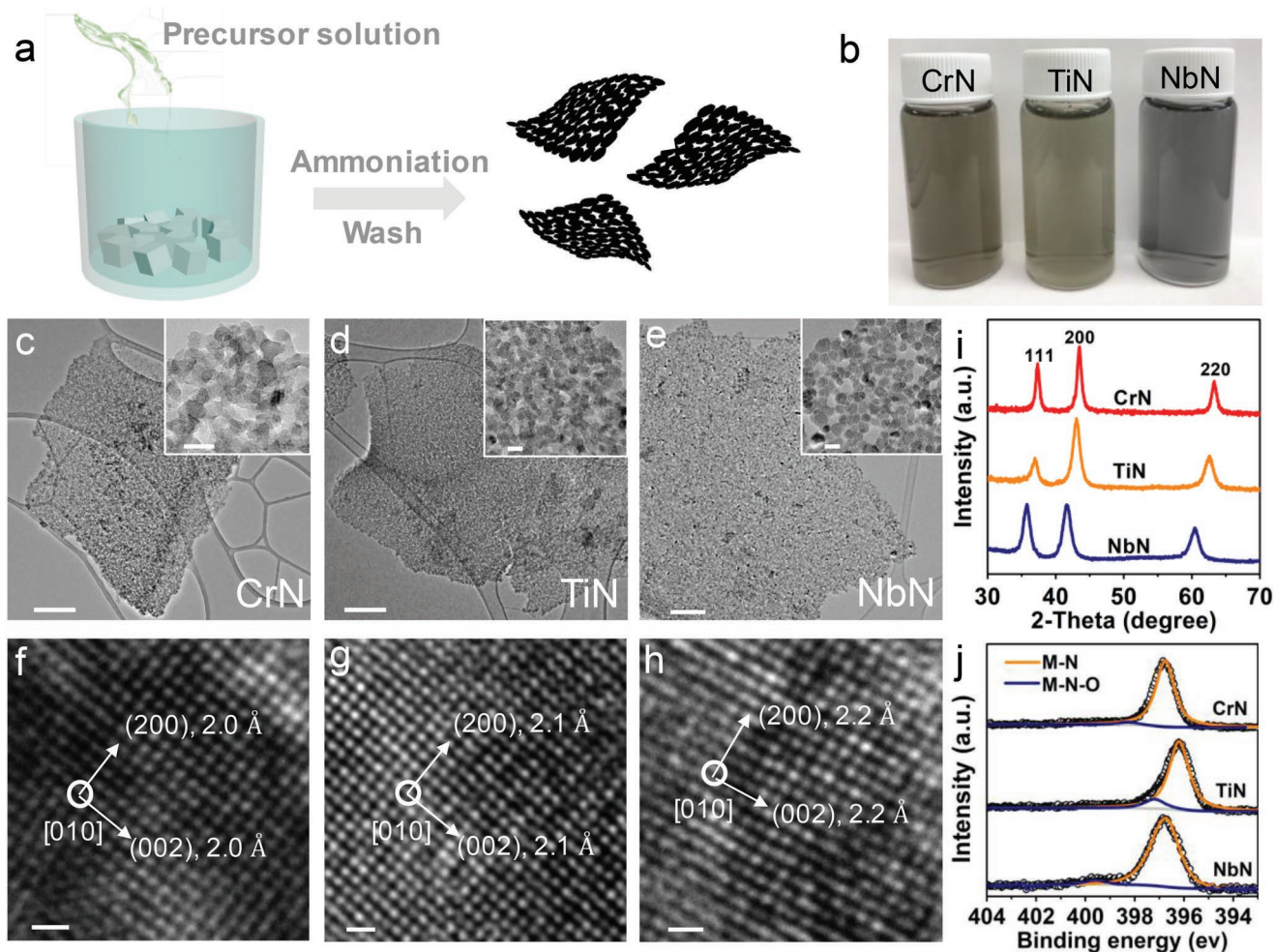**MATERIALS**
www.advmat.de

Figure 1. Synthesis and characterizations of 2D arrays of TMN nanocrystals. a) Schematic of synthesis. The precursor solution in ethanol was poured into 100 g of a salt template. After stirring and drying in an oven at 70 °C, a thin layer of precursor was formed on the surface of salts (labeled as precursor@salt). Then the precursor@salt powder was treated in a furnace at 700–750 °C under a constant flow of ammonia. Finally, after dissolving the salt-template in deionized water (which can be collected and recycled), 2D arrays of TMN nanocrystals were obtained. b) Digital optical images of colloidal solutions of TMN nanocrystals dispersed in deionized water. c–e) TEM images of the 2D arrays of TMN nanocrystals. Scale bars are 200 nm for (c) and (e), and 500 nm for (d). The insets show that 2D flakes are made of interconnected TMN nanocrystals. Scale bars are 10 nm. f–h) HRTEM images of TMN nanocrystals shown in (c–e). Scale bars are 5 Å. i) XRD patterns of 2D arrays of TMN nanocrystals. j) N 1s XPS spectra of 2D arrays of TMN nanocrystals.

a nanostructure that takes advantages of both 0D and 2D morphologies may enable optimal conductivity and accessibility simultaneously. We propose that interconnected few-nanometer TMN nanocrystals with overall 2D morphology would be a promising candidate, providing both high surface area and good electron/ion transport.

In this work, we report on synthesis of various 2D arrays of few-nanometer TMN nanocrystals. Using topochemical synthesis, a thin layer of precursor on the surface of salt template was gradually transformed to TMN under a constant flow of ammonia. During ammoniation, the precursor was "etched" and recrystallized to form interconnected nanocrystals with few-nanometer size, arranged in 2D arrays. The schematic of synthesis is shown in **Figure 1**a. Precursor-coated salts (labeled as precursor@salts) were first prepared by coating a precursor solution in ethanol onto the surface of the salt and drying at 70 °C in air. Here, precursors that can be directly ammoniated

were chosen, which include chromium chloride, titanium ethoxide, and niobium ethoxide, to later yield chromium nitride, titanium nitride, and niobium nitride, respectively. Each precursor@salt was heated separately under a constant flow of ammonia for 2 h and transformed into a TMN@salt with a blackish color. With further washing of the salts in deionized water (DI water), 2D arrays of TMN nanocrystals could be separated and dispersed in solvents. Interestingly, although the color of concentrated solutions of various TMN nanocrystals are all black, their diluted colloidal solutions show different colors due to different electronic and optical properties of the synthesized nitrides (Figure S1, Supporting Information). As shown in Figure 1b, the colors are grayish, yellow-greenish, and blackish for CrN, TiN, and NbN, respectively.

The morphologies of the TMN nanocrystals were investigated by transmission electron microscopy (TEM). As shown in Figure 1c–e, the overall morphologies are ultrathin flakes

**ADVANCED
SCIENCE NEWS**

www.advancedsciencenews.com

**ADVANCED
MATERIALS**

www.advmat.de

with lateral sizes varying from hundreds of nanometers to a few microns. Through atomic force microscopy (AFM) measurements, the thicknesses were estimated to be between 4 and 8 nm (Figure S2, Supporting Information). Impressively, according to magnified TEM images (the insets of Figure 1c–e), these TMN flakes are actually "pseudo" 2D flakes consisting of many interconnected few-nanometer nanocrystals. Statistically, the average domain size of each CrN nanocrystal is 4.7 nm, which is the smallest among the three TMNs samples (Figure S3, Supporting Information), when compared to 6.9 nm of TiN and 7.8 nm of NbN, respectively. This unique structure of 2D arrays of few-nanometer nanocrystals can provide more exposed active sites and allow ionic transport through the flakes due to the presence of pores between the nanocrystals. As shown in Figure S4, Supporting Information, the specific surface areas (SSA) were estimated to be 153, 57, and 88 m^2 g^{-1} for CrN, TiN, and NbN, respectively.

The microscopic crystal structures were further characterized by high-resolution TEM (HRTEM) as shown in Figure 1f–h and Figure S5, Supporting Information. Notably, each few-nanometer nanocrystal is single-crystalline. Two perpendicular lattice planes with d-spacings of 2.0 Å are shown in Figure 1f, which is in accordance with the theoretical d-spacing values of (200) and (002) facets of CrN with a square symmetry on the [010] zone axis (PDF #03-065-2899). The same square symmetries on the [010] zone axes were also visualized for both TiN and NbN, with slightly larger d-spacing values of (200) and (002) facets as shown in Figure 1g,h (PDF #38-1420 and PDF #01-088-2404), which is possibly due to the larger atom sizes of Ti and Nb when compared to Cr. The crystal structures of three TMN nanocrystals were also characterized by X-ray diffraction (XRD). As shown in Figure 1i, three predominant peaks can be indexed to the cubic single-metal nitrides, which is consistent with HRTEM analysis. In addition, the chemical compositions of 2D arrays of TMN nanocrystals were probed by X-ray photoelectron spectroscopy (XPS). The predominant peaks in N 1s region (396.8 eV for CrN, 396.2 eV for TiN, and 396.8 eV for NbN) were assigned to metal-N bonding, confirming the formation of metal nitrides (Figure 1j). Another small peak next to metal-N bonding was assigned to metal-N-O bonding, which can be further confirmed in the metal region as shown in Figure S6, Supporting Information. The existence of O should be attributed to the oxygen termination of TMN surface.[15]

To obtain a more quantitative atomic structure of the materials, X-ray pair distribution function (PDF) analysis was performed on these 2D arrays of TMN nanocrystals. The PDF describes the probability of finding two atoms in a material at a distance r apart and can be used to model the local structure of nanocrystals.[16–21] The data acquisition, data reduction, and structural modeling are described in more detail in Supporting Information. As shown in **Figure 2**, after comparing the measured PDF results with PDF profiles computed from best-fit structural models, all three samples are shown to agree well with cubic TMN structures. Peaks in the PDF show interatomic bonding in the material. For instance, the first peaks around 2 Å in the three profiles further confirmed the presence of metal-N bonds. The cubic lattice parameters obtained after the structure refinement were 4.148 Å for CrN, 4.195 Å for TiN, and 4.318 Å for NbN (See details in Table S1, Supporting Information).
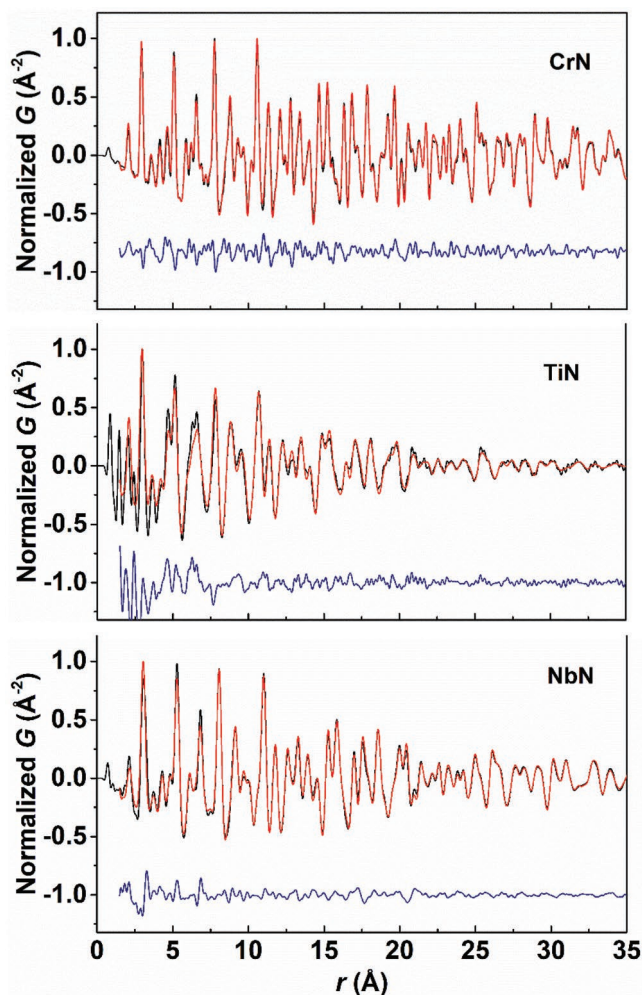

Figure 2. X-ray PDF analysis of 2D arrays of TMN nanocrystals. The black line is the experimentally determined PDF, the red line is the PDF of the best-fit model obtained from the proposed crystal structure. The navy line showing offset below the data is the difference between fitting results and experimental data.

In addition, the X-ray PDF analysis can provide more specific information on crystallinity. Significantly, although the XRD patterns of all the three samples are very similar, their local structure PDF profiles are different. The PDF peaks of CrN and NbN are very sharp, while those of TiN are broad. Furthermore, the PDF signal extended to ≈8 nm for CrN, 6 nm for NbN, but only to 3.5 nm for TiN. Both the broader peaks and the narrower r-range with respect to TiN indicates that CrN and NbN have a higher crystallinity and a much lower level of positional disorder than TiN. We believe this phenomenon can be attributed to the higher reactive surface of low-dimensional TiN, and that a larger amount of oxygen-termination exists on the surface of 2D arrays of TiN than CrN and NbN, and maybe some oxygen dissolved in the lattice to form oxynitrides, resulting in lower structure ordering.

The growth mechanism of the 2D arrays of TMN nanocrystals was studied by comparing the morphology, crystal structure, and chemical composition of samples ammoniated at the same dwell time, but different temperatures. Using CrN as an
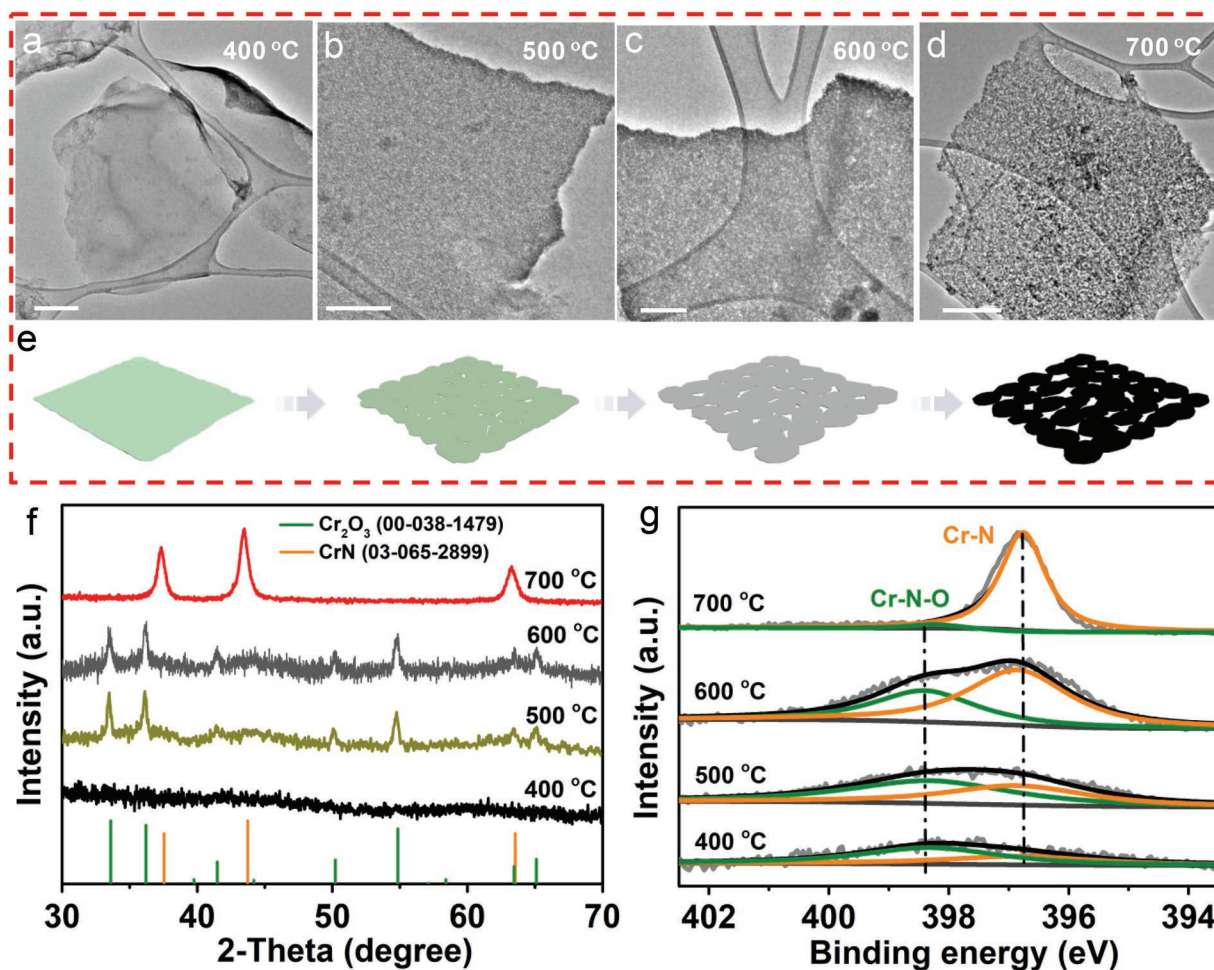
**ADVANCED
SCIENCE NEWS**

www.advancedsciencenews.com

**ADVANCED
MATERIALS**

www.advmat.de

Figure 3. Growth mechanism of 2D arrays of TMN nanocrystals. a–d) TEM images show the morphology change during treatment. Samples were ammoniated at different temperatures, but same dwell time, followed by dissolution of the salt templates. Scale bar: 200 nm. e) Schematic of the changes of morphology at different temperatures. f) XRD and g) XPS analyses of the samples treated at different temperatures.

example, when ammoniating a precursor at 400 °C, light green powders were obtained. A 2D nanosheet morphology, instead of 2D arrays of nanocrystals was achieved, as confirmed by TEM shown in **Figure 3**a. However, no obvious peaks were found in the XRD pattern (Figure 3f) while Cr–O bonding was verified in XPS (Figure S7, Supporting Information), implying the formation of amorphous CrO_x at this stage. Interestingly, two weak Cr–N and Cr–N–O bonding peaks appeared in the N 1s region of XPS (Figure 3g), demonstrating the beginning of ammonation and partial oxygen substitution by nitrogen. When increasing the temperature to 500 °C, 2D arrays started to appear, as shown in Figure 3b,e. According to XRD pattern, all the peaks can be indexed to Cr_2O_3 (PDF #38-1479). Even though there is no phase of chromium nitride, the intensity of Cr–N bonding in XPS is enhanced, resulting from the further substitution of O by N (Figure 3g). This trend is evident when the ammonation temperature increased to 600 °C. The XRD peaks are a little broader than in the pattern obtained at 500 °C (Figure 3f), validating that the domain size of the nanocrystal has decreased, which is in agreement with TEM results (Figure 3c). Although there are still 2D arrays of Cr_2O_3 (Figure 3c,f), the Cr–N bonding becomes predominant

in the XPS spectrum (Figure 3g and Figure S7, Supporting Information). Notably, the color of the sample treated at 600 °C changed from the typical greenish color of Cr_2O_3 to greyish. Finally, blackish powder was obtained after ammonation at 700 °C. At this stage, Cr_2O_3 was completely transformed to CrN, as confirmed by XRD (Figure 3f). Combined with a very strong Cr–N bonding, the formation of 2D arrays of few-nanometer CrN nanocrystals has been verified (Figure 3d,g). Gibbs energy minimization analysis was also conducted to help determine the temperature range for synthesis of CrN. Theoretically, with the reactants being the precursor $CrCl_2$ and the gaseous NH_3 in a 1: 1 molar ratio, several products may form, and yield of nitrides increases as the reaction temperature increases (Figure S8, Supporting Information). CrN appears around 300 °C, but its equilibrium concentration increases slowly before 400 °C, then increases until 900 °C. This is consistent with our observation that only a low percentage of Cr–N bonding was detected at 400 °C, while the precursor completely transformed to CrN at 700 °C.

To summarize, the growth of 2D arrays of TMN nanocrystals is a topochemical synthesis process. During the heating, ultrathin transition metal oxide (TMO) flakes were first

generated. Meanwhile, oxygen was topochemically substituted by nitrogen via ammoniation. Given the intense reaction occurred in pure anhydrous ammonia and noting the huge differences in crystal structures and volumes between TMOs and TMNs, TMOs flakes were "etched" and recrystallized to few-nanometer TMN nanocrystals while retaining the overall 2D morphology. As a comparison, previously, when we used NH_3/Ar mixed gas for topochemical synthesis, the reaction resulted in single-crystalline 2D TMN flakes.[4] In addition, control experiments were used to validate our assumption. As shown in Figure S9, Supporting Information, only nanosheets were obtained when annealing the precursor in air and Ar at 700 °C, demonstrating that the formation of 2D arrays of TMN nanocrystals occurred during ammoniation. These 2D arrays of few-nanometer TMN nanocrystals should be superior to self-assembled nanoparticles, in terms of the conductivity due to interconnected nanocrystals (255 S m^{-1} for CrN, 250 S m^{-1} for TiN, and 261 S m^{-1} for NbN, respectively. See details in Supporting Information).

We hypothesized that this structure may be favorable for applications requiring abundant active sites and high conductivity, such as electrochemical energy storage systems. As we mentioned, TMNs have shown promising performance in Li–S batteries,[7,22] but long-term stability and high areal sulfur loading still need to be addressed. More specifically, poor cycle life and low utilization of sulfur are the main bottlenecks restricting the commercialization of Li–S batteries. Ideally, sulfur cathode hosts for Li–S batteries should have the following characteristics: i) strong surface affinity and high polar binding capability for polysulfides to suppress polysulfide shuttle effect; ii) high specific surface area to ensure uniform dispersion of active sulfur and provide high-density exposed active sites for

the chemical adsorption with polysulfides even at a high sulfur loading (>5 mg cm^{-2}); iii) high conductivity to endow an effective ion and electron pathway for long-term charge/discharge stability of the electrode at high current density. In our case, few-nanometer TMN nanocrystals can provide high surface area with potentially strong affinity of polysulfides, which would be favorable for fast ion diffusion and stable Li-S cathode at high sulfur loading. Moreover, 2D arrays of an interconnected structure can assure fast electron transport in between nanocrystals. Meeting the criteria for ideal Li-S cathode host materials, 2D arrays of TMN nanocrystals are expected to achieve highly stable Li-S battery performance with high areal mass loading.

We first investigated their absorption ability of polysulfides (Li_2S_6) (see details in Supporting Information).[22] The strong surface affinity for polysulfides can be directly verified in optical images (the inset in **Figure 4**a and Figure S10, Supporting Information). For example, 2D arrays of NbN could de-color the polysulfide solution within 5 min (20 mg of TMN nanocrystals powder was soaked in 10 mL of 5 mM Li_2S_6 solution at 25 °C), indicating fast and strong polysulfide adsorption capability. This result can be attributed to the unique structure of 2D arrays of TMN and the intrinsic strong absorption ability of TMN as shown in the previous theoretic calculations.[6] Ultraviolet/visible absorption measurements were conducted to probe the concentration changes of Li_2S_6 solutions as shown in Figure 4a. It can be seen from the static test that the absorption peak of Li_2S_6 in the visible light range (400 nm) disappeared after adding NbN powder for 5 min. Such a strong chemical interaction between TMN nanocrystals and polysulfides should be beneficial to restrain the polysulfide shuttle effect during long-term cycling.
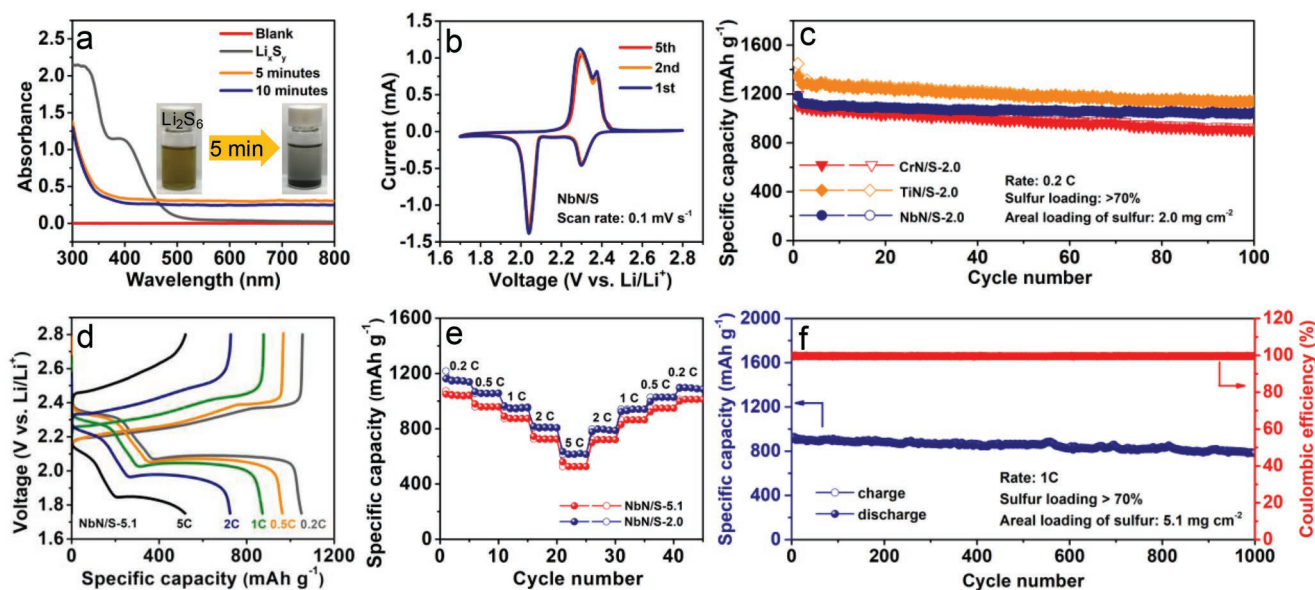

Figure 4. Li–S battery performance of 2D arrays of TMN nanocrystals/sulfur composites. a) Ultraviolet/visible absorption spectra of a Li_2S_6 solution before and after the addition of 2D arrays of NbN nanocrystal powder for 5 and 10 min. It should be noted that the absorption background deviation is due to the particle scattering. The insets show optical images of Li_2S_6 solution before and 5 min after the addition of NbN nanocrystal powder. b) Cyclic voltammetry curves of a Li–S cell with an NbN/S cathode at a scan rate of 0.1 mV s^{-1}. c) Cycling performance of Li–S cells with CrN/S, TiN/S, and NbN/S cathodes at 0.2 C for 100 cycles (1 C = 1674 mA g^{-1}). d) Charge/discharge profiles of a NbN/S cathode with 5.1 mg cm^{-2} sulfur loading at rates from 0.2 to 5 C. e) Rate capability of NbN/S-2.0 and NbN/S-5.1 cathodes at rates from 0.2 to 5 C. f) Cycling performance of NbN/S-5.1 cathode at 1 C for 1000 cycles.

**ADVANCED
SCIENCE NEWS**
www.advancedsciencenews.com

**ADVANCED
MATERIALS**
www.advmat.de

Accordingly, three TMN/S composites were fabricated by a melting diffusion method (see details in Supporting Information).[23] The sulfur loading percentages in all three composites are higher than 70 wt% (NbN/S: 73.15 wt%; TiN/S: 71.55 wt%; and CrN/S: 71.24 wt.%) as determined by thermogravimetric analysis (TGA; Figure S11, Supporting Information). The chemical compositions were confirmed by XRD, elemental mapping, and XPS (see details in Figure S12–S14, Supporting Information). First, the electrochemical performance of three composites was studied by assembling coin cells with an areal sulfur loading of 2.0 mg cm^{-2} (labeled as TMN/S-2.0). As shown in Figure 4b and Figure S15, Supporting Information, two representative cathodic peaks can be found in the cyclic voltammetry (CV) curves with no obvious shift within the initial five cycles. These peaks are attributed to the formation of long-chain polysulfides (Li$_2$S$_x$, $4 < x \leq 8$) from S$_8$, and subsequently the formation of short-chain sulfides (Li$_2$S$_2$ and Li$_2$S), respectively. The anodic peaks demonstrated the reversible conversion.[24] All the three electrodes showed high initial reversible capacities and NbN/S has the best cycling stability (Figure 4c; Figure S16 and Table S2, Supporting Information). After 100 cycles at 0.2 C (1C = 1674 mA g^{-1}), 93 % of the reversible capacity of 1140 mAh g^{-1} was retained. When cycling at 0.5 C for 300 cycles, only 7.7% of capacity was lost and the voltage plateau showed no change (Figure S17a, Supporting Information). NbN/S with a cycling performance of 0.026% degradation per cycle at 0.5 C represents one of the most stable sulfur cathode hosts and is superior to various transition metal oxide/sulfide (TMO/TMS),[25–28] TMN,[22,29] and carbon-based cathodes[8,30] with similar sulfur loading reported in literature (Table S2, Supporting Information).

In practice, a higher areal sulfur loading (>5 mg cm^{-2}) is highly demanded for Li–S batteries.[8] In this context, we focused on the most stable NbN/S electrode and fabricated a higher areal sulfur loading electrode of 5.1 mg cm^{-2} (labeled as NbN/S-5.1). As shown in Figure 4d and Figure S17b, Supporting Information, the NbN/S-5.1 electrode shows good rate performance and high Coulombic efficiency at scan rates ranging from 0.2 to 5 C, similar to the NbN/S-2.0 electrode. It should be noted that NbN/S-5.1 is working well even at a high rate of 5 C, as the discharge plateau is still obvious and stable. Reversible and stable capacities of 1050 mAh g^{-1}, 979 mAh g^{-1}, 905 mAh g^{-1}, 745 mAh g^{-1}, and 560 mAh g^{-1} are obtained at 0.2, 0.5, 1, 2, and 5 C, respectively, which are only slightly lower than the capacities of NbN-2.0 electrodes without obvious capacity degradation (Figure 4e), demonstrating the excellent stability of the NbN-5.1 electrodes at different rates. Impressively, as shown in Figure 4f, the NbN/S-5.1 electrode delivered an initial capacity of 912.8 mAh g^{-1} and retained a high capacity of 796.5 mAh g^{-1} (87.3 % of the initial capacity) with the stable capacity retention over 1000 cycles at 1C (a slow degradation rate of 0.013% per cycle). To date, for most of the reported works, the long-term cycling test is generally carried out at a lower sulfur-loading due to the limited carbon-polysulfides or metal-polysulfides interaction interfaces in 0D, 1D, and 2D sulfur hosts materials (such as CNT, graphene, TMOs, and other TMNs).[8,25,30] To the best of our knowledge, this high-rate cycling performance of the NbN/S-5.1 electrode is the best among slurry-based cathodes[6,8] and many self-supporting

cathodes with similar sulfur loading.[30,31] The detailed comparison is presented in Table S2, Supporting Information.

Additionally, several control experiments were conducted to directly prove the advantage of 2D arrays of TMN nanocrystals over 0D and 2D particles. To enable the comparison, all of the electrodes were fabricated with the areal sulfur loading of ≈5.1 mg cm^{-2} using the same assembly process and conditions. N-doped Ti$_3$C$_2$ MXene and reduced graphene oxide (RGO) were used as representative 2D materials. RGO showed the highest initial capacity (1000 mAh g^{-1}) but degraded quickly already after 100 cycles (Figure S18, Supporting Information), which could be due to a limited affinity of polysulfides to carbon. N-doped Ti$_3$C$_2$ MXene showed a stable performance, but the reversible capacity was below 700 mAh g^{-1}, which is much lower than for 2D arrays of NbN. CrN, NbN, and TiN nanoparticles were also tested (Figures S18 and S19, Supporting Information). All of them showed pretty stable performance, which again demonstrated the good affinity of polysulfides to TMNs. However, the reversible capacities were below 600 mAh g^{-1}. This is probably because agglomerated TMN nanoparticles have a lower electronic and ionic conductivity.

The performance of the high sulfur loading electrodes emphasizes the synergistic effect of high surface area, high-density active sites, inherently strong polysulfides affinity, and high conductivity of the 2D arrays of TMN nanocrystals. The high specific surface area that resulted from the 2D arrays can keep the uniform distribution of large amounts of sulfur species, while strong interactions between them assure the stable trapping and reversible conversion of large amounts of polysulfides during long-term cycling. After several cycles, the surface chemistry of a NbN/S electrode was checked when discharged to 1.7 V. As shown in Figure S14, Supporting Information, compared to the initial NbN/S electrode, the predominant S 1s peak (162.1 eV) was Li$_2$S, which demonstrated the reversible electrochemical conversion process during the charge/discharge cycling.[32–35] Combined with the fast ion and electron transport provided by the interconnected 2D arrays of TMN nanocrystals, high mass loading cathodes can work at high rates, showing high capacity during charge/discharge cycling. Interestingly, given the good conductivity of 2D arrays of TMN nanocrystals, we also fabricated an NbN/S electrode without carbon black conductive additive. As shown in Figure S20, both capacity and stability are similar to the traditional electrode with carbon black, implying the total volumetric capacity may be further increased by eliminating traditional conductive additive.

In conclusion, we report a general approach for high-yield synthesis of interconnected 2D arrays of few-nanometer TMN nanocrystals. Based on systematic analysis, we propose a topochemical synthesis mechanism. Because of the reaction with ammonia and the differences in crystal structures and volumes of TMOs and TMNs, during the synthesis, the initially formed TMOs were etched and topochemically transformed to interconnected few-nanometer TMN nanocrystals while retaining a 2D-like morphology. Such a unique structure provides high surface area and high conductivity as demonstrated in Li–S batteries. Combined with inherently strong interactions with sulfur species, 2D arrays of NbN nanocrystals-based electrodes show an ultra-stable and high specific capacity during 1000 cycles under high areal sulfur loading, which may effectively mitigate

the issue of the polysulfide shuttle effect. With deeper understanding of the underlying growth process, 2D arrays of TMN, or maybe even transition metal carbide and boride nanocrystals, may be produced with versatile properties and broad applications beyond energy storage.

Conflict of Interest

The authors declare no conflict of interest.

[1] Z. Y. Al Balushi, K. Wang, R. K. Ghosh, R. A. Vilá, S. M. Eichfeld, J. D. Caldwell, X. Qin, Y.-C. Lin, P. A. DeSario, G. Stone, S. Subramanian, D. F. Paul, R. M. Wallace, S. Datta, J. M. Redwing, J. A. Robinson, *Nat. Mater.* **2016**, *15*, 1166.

[2] G. V. Naik, J. L. Schroeder, X. Ni, A. V. Kildishev, T. D. Sands, A. Boltasseva, *Opt. Mater. Express* **2012**, *2*, 478.

[3] J. Xie, S. Li, X. Zhang, J. Zhang, R. Wang, H. Zhang, B. Pan, Y. Xie, *Chem. Sci.* **2014**, *5*, 4615.

[4] X. Xiao, H. Yu, H. Jin, M. Wu, Y. Fang, J. Sun, Z. Hu, T. Li, J. Wu, L. Huang, Y. Gogotsi, J. Zhou, *ACS Nano* **2017**, *11*, 2180.

[5] Z. Liu, R. Beaulac, *Chem. Mater.* **2017**, *29*, 7507.

[6] Q. Pang, X. Liang, C. Y. Kwok, L. F. Nazar, *Nat. Energy* **2016**, *1*, 16132.

[7] Z. Cui, C. Zu, W. Zhou, A. Manthiram, J. B. Goodenough, *Adv. Mater.* **2016**, *28*, 6926.

[8] G. Tan, R. Xu, Z. Xing, Y. Yuan, J. Lu, J. Wen, C. Liu, L. Ma, C. Zhan, Q. Liu, T. Wu, Z. Jian, R. Shahbazian-Yassar, Y. Ren, D. J. Miller, L. A. Curtiss, X. Ji, K. Amine, *Nat. Energy* **2017**, *2*, 17090.

[9] H. Pan, J. Chen, R. Cao, V. Murugesan, N. N. Rajput, K. S. Han, K. Persson, L. Estevez, M. H. Engelhard, J.-G. Zhang, K. T. Mueller, Y. Cui, Y. Shao, J. Liu, *Nat. Energy* **2017**, *2*, 813.

[10] G. A. DeVries, M. Brunnbauer, Y. Hu, A. M. Jackson, B. Long, B. T. Neltner, O. Uzun, B. H. Wunsch, F. Stellacci, *Science* **2007**, *315*, 358.

[11] H.-E. Lee, H.-Y. Ahn, J. Mun, Y. Y. Lee, M. Kim, N. H. Cho, K. Chang, W. S. Kim, J. Rho, K. T. Nam, *Nature* **2018**, *556*, 360.

[12] X. Sang, Y. Xie, M. W. Lin, M. Alhabeb, K. L. Van Aken, Y. Gogotsi, P. R. C. Kent, K. Xiao, R. R. Unocic, *ACS Nano* **2016**, *10*, 9193.

[13] M. R. Lukatskaya, S. Kota, Z. Lin, M. Q. Zhao, N. Shpigel, M. D. Levi, J. Halim, P. L. Taberna, M. W. Barsoum, P. Simon, Y. Gogotsi, *Nat. Energy* **2017**, *2*, 17105.

[14] M. R. Lukatskaya, O. Mashtalir, C. E. Ren, Y. D. Agnese, P. Rozier, P. L. Taberna, M. Naguib, P. Simon, M. W. Barsoum, Y. Gogotsi, *Science* **2013**, *341*, 1502.

[15] B. Anasori, M. R. Lukatskaya, Y. Gogotsi, *Nat. Rev. Mater.* **2017**, *2*, 16098.

[16] T. Egami, S. J. L. Billinge, *Underneath the Bragg Peaks: Structural Analysis of Complex Materials*, 2nd ed, Elsevier, Amsterdam, the Netherlands **2012**.

[17] P. J. Chupas, X. Qiu, J. C. Hanson, P. L. Lee, C. P. Grey, S. J. L. Billinge, *J. Appl. Crystallogr.* **2003**, *36*, 1342.

[18] C. L. Farrow, P. Juhás, J. W. Liu, D. Bryndin, E. S. Božin, J. Bloch, T. Proffen, S. J. L. Billinge, *J. Phys.: Cond. Matter* **2007**, *19*, 335219.

[19] T. Proffen, S. J. L. Billinge, *J. Appl. Crystallogr.* **1999**, *32*, 572.

[20] P. Juhás, T. Davis, C. L. Farrow, S. J. L. Billinge, *J. Appl. Crystallogr.* **2013**, *46*, 560.

[21] X. Yang, P. Juhás, C. L. Farrow, S. J. L. Billinge, arXiv:1402.3163 **2014**.

[22] Z. Sun, J. Zhang, L. Yin, G. Hu, R. Fang, H. M. Cheng, F. Li, *Nat. Commun.* **2017**, *8*, 14627.

[23] X. Ji, K. T. Lee, L. F. Nazar, *Nat. Mater.* **2009**, *8*, 500.

[24] M. Armand, J. M. Tarascon, *Nature* **2008**, *451*, 652.

[25] X. Tao, J. Wang, C. Liu, H. Wang, H. Yao, G. Zheng, Z. W. Seh, Q. Cai, W. Li, G. Zhou, C. Zu, Y. Cui, *Nat. Commun.* **2016**, *7*, 11203.

[26] J. He, L. Luo, Y. Chen, A. Manthiram, *Adv. Mater.* **2017**, *29*, 1702707.

[27] X. Liu, J. Q. Huang, Q. Zhang, L. Mai, *Adv. Mater.* **2017**, *29*, 1601759.

[28] X.-C. Liu, Y. Yang, J. W, M. Liu, S. P. Zhou, B. D. A. Levin, X.-D. Zhou, H. Cong, D. A. Muller, P. M. Ajayan, H. D. Abruña, F.-S. Ke, *ACS Energy Lett.* **2018**, *3*, 1325.

[29] T. Zhou, W. Lv, J. Li, G. Zhou, Y. Zhao, S. Fan, B. Liu, B. Li, F. Kang, Q. H. Yang, *Energy Environ. Sci.* **2017**, *10*, 1694.

[30] Z. Li, J. T. Zhang, Y. M. Chen, J. Li, X. W. Lou, *Nat. Commun.* **2015**, *6*, 8850.

[31] F. Pei, L. Lin, D. Ou, Z. Zheng, S. Mo, X. Fang, N. Zheng, *Nat. Commun.* **2017**, *8*, 482.

[32] S. Xin, L. Gu, N. H. Zhao, Y. X. Yin, L. J. Zhou, Y. G. Guo, L. J. Wan, *J. Am. Chem. Soc.* **2012**, *134*, 18510.

[33] N. Jayaprakash, J. Shen, S. S. Moganty, A. Corona, L. A. Archer, *Angew. Chem., Int. Ed.* **2011**, *50*, 5904.

[34] M. R. Kaiser, Z. Ma, X. Wang, F. Han, T. Gao, X. Fan, J. Z. Wang, H. K. Liu, S. Dou, C. Wang, *ACS Nano* **2017**, *11*, 9048.

[35] L. Ma, H. Yuan, W. Zhang, G. Zhu, Y. Wang, Y. Hu, P. Zhao, R. Chen, T. Chen, J. Liu, Z. Hu, Z. Jin, *Nano Lett.* **2017**, *17*, 7839.